



# Glacial cycles drive variations in the production of oceanic crust

## Citation

Crowley, J. W., R. F. Katz, P. Huybers, C. H. Langmuir, and S.-H. Park. 2015. Glacial Cycles Drive Variations in the Production of Oceanic Crust. *Science* 347, no. 6227: 1237–1240. doi:10.1126/science.1261508.

## Published Version

doi:10.1126/science.1261508

## Permanent link

<http://nrs.harvard.edu/urn-3:HUL.InstRepos:32097098>

## Terms of Use

This article was downloaded from Harvard University's DASH repository, WARNING: No applicable access license found.

## Share Your Story

The Harvard community has made this article openly available.  
Please share how this access benefits you. [Submit a story](#).

[Accessibility](#)

## OCEANOGRAPHY

# Glacial cycles drive variations in the production of oceanic crust

John W. Crowley,<sup>1,2\*</sup> Richard F. Katz,<sup>1†</sup> Peter Huybers,<sup>2</sup>  
Charles H. Langmuir,<sup>2</sup> Sung-Hyun Park<sup>3†</sup>

Glacial cycles redistribute water between oceans and continents, causing pressure changes in the upper mantle, with consequences for the melting of Earth's interior. Using Plio-Pleistocene sea-level variations as a forcing function, theoretical models of mid-ocean ridge dynamics that include melt transport predict temporal variations in crustal thickness of hundreds of meters. New bathymetry from the Australian-Antarctic ridge shows statistically significant spectral energy near the Milankovitch periods of 23, 41, and 100 thousand years, which is consistent with model predictions. These results suggest that abyssal hills, one of the most common bathymetric features on Earth, record the magmatic response to changes in sea level. The models and data support a link between glacial cycles at the surface and mantle melting at depth, recorded in the bathymetric fabric of the sea floor.

The bathymetry of the sea floor has strikingly regular variations around intermediate and fast-spreading ocean ridges. Parallel to the ridge are long, linear features with quasi-regular spacing called abyssal hills (1). High-resolution mapping of the sea floor over the past few decades (2–4) has shown that these hills are among the most common topographic features of the planet, populating the sea floor over ~50,000 km of ridge length. Hypothesized models for these features include extensional faulting parallel to the ridge (3), variations in the magmatic budget of ridge volcanoes (5), and variation in mantle melting under ridges owing to sea-level change associated with glacial cycles (6). This latter model stems from the fact that glacial-interglacial variations transfer  $\sim 5 \times 10^{19}$  kg of water between the oceans and the continents. This mass redistribution translates to sea-level variations of ~100 m and modifies the lithostatic pressure beneath the entire ocean. Because mantle melting beneath ridges is driven by depressurization, ocean ridge volcanism should respond to sea-level changes, potentially leading to changes in the thickness and elevation of ocean crust.

Plate spreading at mid-ocean ridges draws mantle flow upward beneath the ridge; rising parcels of mantle experience decreasing pressure and hence decreasing melting point, causing partial melting. Mantle upwelling rates are ~3 cm/year on average, whereas sea-level change during the last deglaciation was at a mean rate of 1 cm/year over 10 thousand years (ky). Because water has one third the density of rock, sea-level changes would modify the depressurization rate associated with upwelling by  $\pm 10\%$ , with corresponding effects on the rate of melt production. Mantle

upwelling rate scales with the mid-ocean ridge spreading rate, but the rate of sea-level change over the global mid-ocean ridge system is roughly uniform. On this basis, previous workers inferred that the relative effect of sea-level change should scale inversely with spreading rate, reaching a maximum at the slowest rates (6). An elaboration of this model with parameterized melt transport gave a similar scaling (7).

To test these qualitative inferences, we investigated the crustal response to sea-level change

using a model that computes mantle flow, thermal structure, melting, and pathways of melt transport. The model is based on canonical statements of conservation of mass, momentum, and energy for partially molten mantle (8, 9) and has previously been used to simulate mid-ocean ridge dynamics with homogeneous (10) and heterogeneous (11) mantle composition. It predicts time scales of melt transport that are consistent with those estimated from <sup>230</sup>Th disequilibrium in young lavas (12). In the present work, the model is used to predict crustal thickness time series arising from changes in sea level (Fig. 1) (13).

A suite of nine model runs for three permeability scales and three spreading rates was driven over a 5-million-year period by using a Plio-Pleistocene sea-level reconstruction (14). Crustal curves from simulations with larger permeability and faster spreading rate contain relatively more high-frequency content than those of lower permeability and slower-spreading-rate runs (Fig. 1). Our model results contradict the previous scaling arguments (6, 7) in not showing a simple decrease in the sea-level effect on ridge magmatism with increasing spreading rate.

To better understand these numerical results, we carried out an analysis of leading-order processes using a reduced complexity model. This model provides a solution for crustal thickness response to changes in sea level, approximating the results of the full numerical model, but with greater transparency. Assuming that all melt produced by sea-level change is focused to the

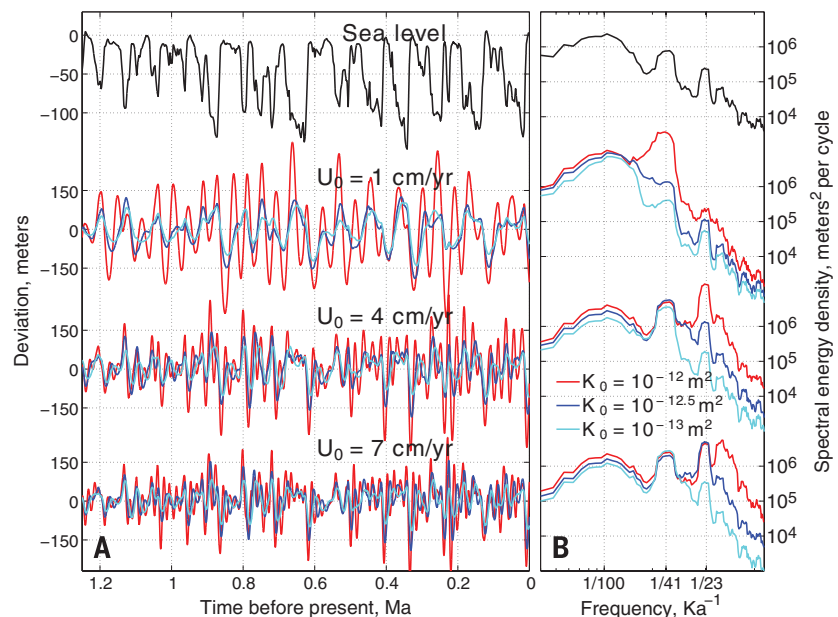


**Fig. 1. Simulated bathymetric relief driven by Plio-Pleistocene sea-level variation.** (A) Imposed sea-level variation [black, from (14)] and predicted bathymetric relief (color) for the past 1.25 million years from simulations at three half-spreading rates  $U_0$  and three permeability levels  $K_0$ . Isostatic compensation is assumed to scale the amplitude of crustal thickness variation by 6/23 to give bathymetric relief. Permeability in the simulations is computed by applying  $K(x,z) = K_0(\phi/\phi_0)^3$  m<sup>2</sup> to the porosity field  $\phi(x,z)$ , where  $\phi_0 = 0.01$  is a reference porosity. Light blue, dark blue, and red lines correspond to  $\log_{10} K_0 = (-13, 12.5, 12)$ , respectively. (B) Power spectral density estimates for each time series, made by using the multitaper method with seven tapers. Axes are logarithmic.

<sup>1</sup>Department of Earth Sciences, University of Oxford, Oxford, UK. <sup>2</sup>Department of Earth and Planetary Sciences, Harvard University, Cambridge, USA. <sup>3</sup>Division of Polar Earth-System Sciences, Korea Polar Research Institute, Incheon, Korea. \*Present address: Engineering Seismology Group Canada, Kingston, Canada. †Corresponding author. E-mail: richard.katz@earth.ox.ac.uk (R.F.K.); shpark314@kopri.re.kr (S.-H. P.)

ridge axis, we obtain a magmatic flux in units of kilograms per year per meter along the ridge of

$$M_{SL}(t) = \int_{z_m}^0 x_l(z) \frac{\rho_w}{\rho_m} \Pi \dot{S}[t - \tau(z)] dz \quad (1)$$

where  $\rho_w/\rho_m$  is the density ratio of sea water to mantle rock,  $\Pi$  is the adiabatic productivity of upwelling mantle (in kilograms of melt per cubic meter of mantle per meter of upwelling),  $x_l(z)$  is the half-width of the partially molten region beneath the mid-ocean ridge at a depth  $z$ ,  $z_m$  is the maximum depth of silicate melting beneath the ridge, and  $\dot{S}[t - \tau(z)]$  is the rate of sea-level change  $\tau$  years before time  $t$  (13).

This formulation reveals why our numerical model results (Fig. 1) contradict earlier work (6, 7). Whereas earlier work noted that variations in crustal thickness are inversely proportional to spreading rate,  $C_{SL} = M_{SL}/(U_0\rho_c)$ , our model shows that mass flux is proportional to the width of the partially molten region beneath the ridge. This width can be expressed as  $x_l(z) = U_0R(z)/(4\kappa)$ , where  $U_0$  is the half-spreading rate,  $\kappa$  is the thermal diffusivity, and  $R(z)$  accounts for depth-dependent influences on melting that are independent of spreading rate (fig. S1). The competing influences associated with the volume of mantle from which melt is extracted and the rate at which new crust is formed means that sensitivity to sea-level variation does not simply decrease with increasing spreading rate.

Instead, the magnitude of the crustal response depends on the time scale of sea-level forcing relative to the time required to deliver melt from depth to the surface. Melt delivery times  $\tau$  are computed in the reduced model by using a one-dimensional melt column formulation and decrease with higher permeability and faster spreading rate (13, 15). The same response occurs in the numerical model; in both cases,  $\tau$  decreases with increasing spreading rate because the background melting rate, dynamic melt fraction, and permeability of the melting region all increase.

To quantify crustal response as a function of time scale, we use the amplitude ratio of crustal to sea-level variation, called admittance, computed at discrete frequencies by applying sinusoidal forcing. Admittance curves for both the numerical (Fig. 2A) and reduced (Fig. 2B) models show a distinct maximum that shifts toward higher frequencies and larger magnitudes with shorter  $\tau$ . When the period of sea-level forcing is short relative to the characteristic transport time  $\tau_m = \tau(z_m)$ , additional melt produced at depth (falling sea-level phase) does not have time to reach the surface before a negative perturbation to melt production occurs (rising sea-level phase); positive and negative perturbations cancel, and crustal variation is small. When forcing periods are long relative to  $\tau_m$ , melt perturbations reach the surface but are again small because melt production scales with the rate-of-change of sea level. Forcing periods near  $\tau_m$  give maximum admittance because of a combination of large perturbation of melting rates and sufficient time to reach the surface (Fig. 2C). These results suggest that ridges are tuned according to melt-

transport rates to respond most strongly to certain frequencies of sea-level variability.

The correspondence of the results from the numerical and reduced models provides a sound basis for investigating the potential effects of sea-level change on sea-floor bathymetry. Variations in melt production lead to variations in crustal thickness, and through isostatic compensation, such thickness variations should produce changes in bathymetry identifiable in high-resolution surveys. The prominent spectral peaks of late Pleistocene sea-level variation at the approximately  $1/100 \text{ ky}^{-1}$  ice age,  $1/41 \text{ ky}^{-1}$  obliquity, and  $1/23 \text{ ky}^{-1}$  precession frequencies (16) therefore translate into a prediction for a bathymetric response that depends on permeability and spreading rate.

Our model results suggest that the best chance to detect a sea-level response between  $1/100 \text{ ky}^{-1}$  to  $1/20 \text{ ky}^{-1}$  frequencies is at intermediate spreading ridges. Slow spreading ridges show little precession response, an obliquity response that is sensitive to uncertainties in permeability, and the effects of intense normal faulting. Such faulting causes rift valleys with larger relief than expected from sea level-induced melting variations. The sea-level signal should be less polluted by tectonic effects at fast spreading ridges but may have peak admittances at frequencies higher than

$1/20 \text{ ky}^{-1}$  that would obscure the responses at predicted frequencies. For example, the numerical simulation with the fastest spreading and highest permeability has peak spectral energy at frequencies above precession (Fig. 1B).

At intermediate half-spreading rates of 3 cm/year, 40-ky periods lead to predicted bathymetric variations with a wavelength of 1200 m on each side of the ridge. Such fine-scale variations can be obscured in global topographic databases that grid data from multiple cruises and may have offsets in navigation or depth. To investigate the model predictions, a modern data set with uniform navigation and data reduction from a single survey is preferred. Such data are available for two areas of the Australian-Antarctica ridge that were surveyed by the icebreaker Araon of the Korean Polar Research Institute in 2011 and 2013 (Fig. 3).

Analysis was undertaken by identifying a region whose abyssal hill variability is relatively undisturbed by localized anomalies, averaging off-axis variability into a single bathymetric line and converting off-axis distance into an estimate of elapsed time by using a plate motion solution (17). Spectral analysis of the associated bathymetry time series is performed by using the multitaper procedure (18) and shows spectral peaks that are significant at an ~95% confidence level

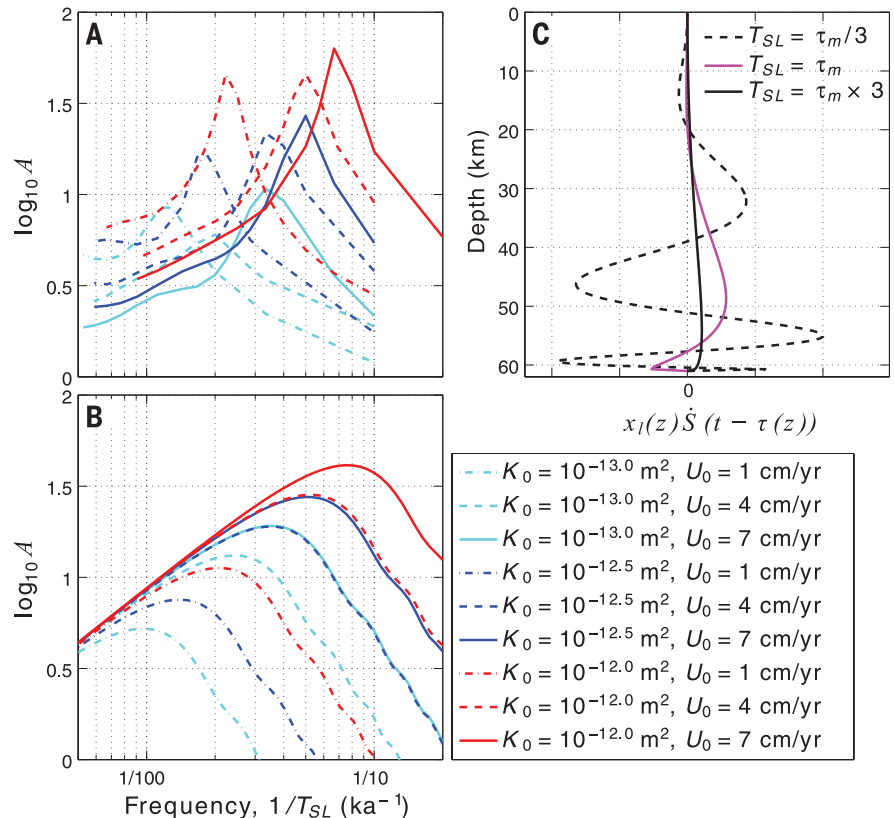


**Fig. 2. Crustal thickness admittance, computed for a sinusoidal variation in sea level with period  $T_{SL}$ .** (A and B) Admittance curves derived from (A) numerical simulations and (B) the reduced model (13). (C) A plot of depth  $z$  versus the integrand from the reduced model of magma production owing to sea-level variation,  $M_{SL}(t) \propto \int_{z_m}^0 x_l(z) \dot{S}[t - \tau(z)] dz$  (Eq. 1 and text following). The model is evaluated for  $U_0 = 4 \text{ cm/year}$ ,  $K_0 = 10^{-13} \text{ m}^2$ , and three values of sea-level oscillation period  $T_{SL}$ .

near the predicted ice age, obliquity, and precession frequencies (Fig. 3). Although absolute ages are uncertain because we lack sea-floor magnetic reversing data, spectral analysis only requires constraining the relative passage of time. The  $2\sigma$  uncertainties associated with relative Australian-Antarctic plate motion are  $\pm 4\%$  (17), implying, for example, that the  $1/41 \text{ ky}^{-1}$  obliquity signal resides in a band from  $1/39 \text{ ky}^{-1}$  to  $1/43 \text{ ky}^{-1}$ , a width that is smaller than our spectral resolution.

Another check on model-data consistency is to compare magnitudes of variability. Surface bathymetry will be roughly  $6/23$ ths of the total variation in crustal thickness because of the relative

density differences of crust-water and crust-mantle, assuming conditions of crustal isostasy. The closest match between simulation results and observations, in terms of the distribution of spectral energy, is achieved by specifying a permeability at 1% porosity of  $K_0 = 10^{-13} \text{ m}^2$  (Fig. 3). The standard deviation of the simulated bathymetry is 36 m, after multiplying crustal thickness by  $6/23$  and filtering (13). To minimize the contribution from non-sea-level-induced variations in the observed bathymetry, it is useful to filter frequencies outside of those between  $1/150 \text{ ky}^{-1}$  and  $1/10 \text{ ky}^{-1}$ . The standard deviation of the filtered observations is 44 m, where the slightly larger

value is consistent with changes in sea level being an important but not exclusive driver of changes in crustal thickness.

Analysis of bathymetry in another area of the Australian-Antarctic ridge 400 km to the southeast (fig. S2) shows a significant spectral peak at the obliquity frequency and indication of a peak near  $1/100 \text{ ky}^{-1}$ , but no peak near the precession frequencies. Predicted and observed bathymetry is also similar, with standard deviations of 33 and 34 m, respectively, after accounting for fractional surface expression and filtering. Absence of a precession peak may result from spectral estimates being more sensitive to elapsed time errors at higher frequencies (19), where such errors may be introduced through extensional faulting or asymmetric spreading. Detection could also be obscured by the previously noted influence of faulting (3, 20) as well as off-axis volcanism or sediment infilling of abyssal troughs. Detection of significant spectral peaks at predicted frequencies at two locations of the Australian-Antarctic ridge nonetheless constitutes strong evidence for modulation of crustal production by variations in sea level.

Our numerical and analytical results show a complex relationship between spreading rate and amplitudes of crustal thickness variations associated with changes in sea level. Perturbations to the background melt production and delivery depend on the frequency content of the sea-level signal, as a result of the dynamics of magma transport. Reference mantle permeability and ridge-spreading rate are key controls on this frequency dependence. This result could be useful: The spreading rate can be accurately determined for a ridge, but parameters associated with magma dynamics are far less certain, such as the amplitude and scaling of permeability. Uncertainty associated with spectral estimates of bathymetry and sea-level estimates need to be better characterized, but together, these may provide a constraint on the admittance and hence dynamical parameters of a ridge.

Although results from the high-resolution bathymetry are promising, much remains to be done to further test the hypothesis advanced here. Crustal thickness is not an instantaneous response to melt delivery from the mantle but also reflects crustal processes that may introduce temporal and spatial averaging. Where long-lived magma chambers are present, for example, there may also be a crustal time-averaging that depends on spreading rate. In addition, faulting at all spreading rates is an observed and important phenomenon, and sea-floor bathymetry reflects the combined effects of magma output and crustal faulting (3, 20). Deconvolving the relative roles of such processes will be important. High-resolution surveys in targeted regions will provide the opportunity for a more complete and rigorous analysis than is presently possible.

#### REFERENCES AND NOTES

1. H. Menard, J. Mammerickx, *Earth Planet. Sci. Lett.* **2**, 465–472 (1967).
2. D. Scheirer et al., *Mar. Geophys. Res.* **18**, 1–12 (1996).

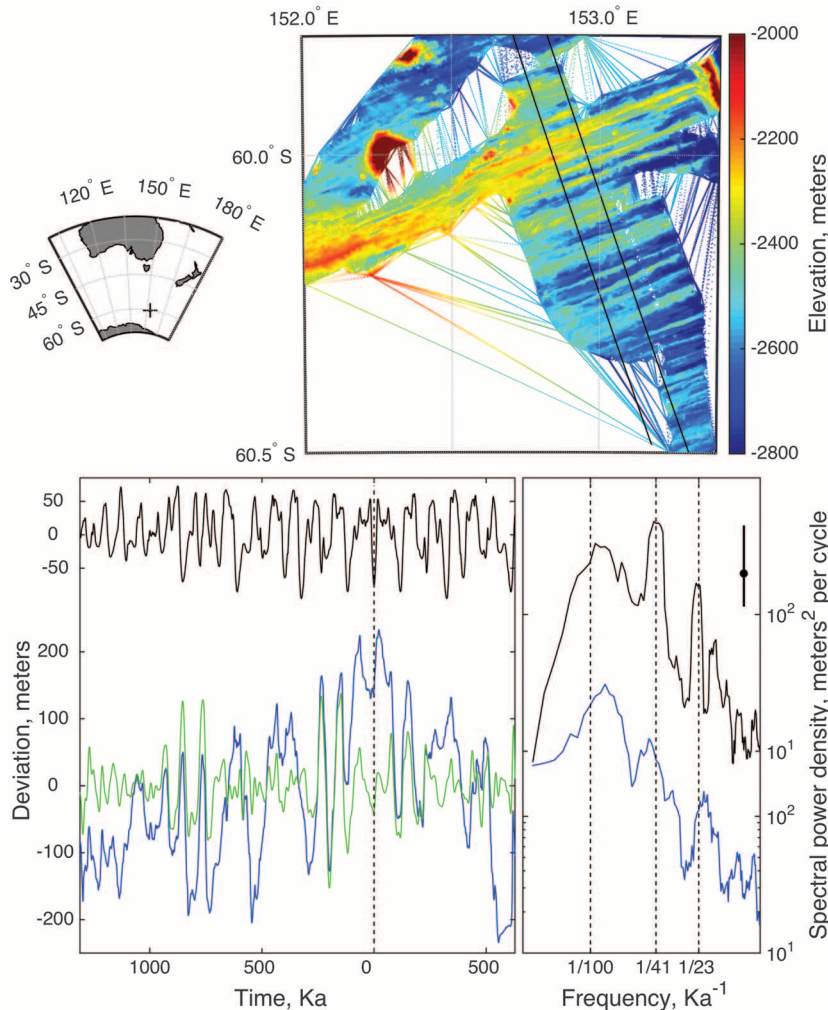


**Fig. 3. Bathymetry at a section of the Australian-Antarctic Ridge.** A region of consistent bathymetry is indicated between the black lines (top right) and is shown in profile (bottom left, blue) after converting off-axis distance to an estimate of time. Time is zero at the approximate ridge center. Also shown is bathymetry after filtering frequencies outside of  $1/150 \text{ ky}$  and  $1/10 \text{ ky}$  (green), and simulated bathymetry (black, for  $U_0 = 3.3 \text{ cm/year}$  and  $K_0 = 10^{-13} \text{ m}^2$ ). Spectral estimates (bottom right) are shown for the unfiltered bathymetry (blue) and model results (black), where the latter are offset upward by an order of magnitude for visual clarity. Data availability is uneven across the ridge, and spectral estimates are for the longer, southern flank. Unlike in Fig. 1B, spectral estimates are prewhitened in order to improve the detectability of spectral peaks (supplementary materials). Vertical dashed lines indicate frequencies associated with 100-ky late-Pleistocene ice ages, obliquity, and precession. Axes are logarithmic. Statistical significance is indicated by the black bar at the top right; spectral peaks rising further than the distance between the mean background continuum (corresponding to the black dot) and 95th percentile (top of black bar) are significant.

3. K. Macdonald, P. Fox, R. Alexander, R. Pockalny, P. Gente, *Nature* **380**, 125–129 (1996).
4. J. Goff, Y. Ma, A. Shah, J. Cochran, J. Sempere, *J. Geophys. Res.* **102** (B7), 15521 (1997).
5. E. Kappel, W. Ryan, *J. Geophys. Res.* **91** (B14), 13925 (1986).
6. P. Huybers, C. Langmuir, *Earth Planet. Sci. Lett.* **286**, 479–491 (2009).
7. D. C. Lund, P. D. Asimow, *Geochem. Geophys. Geosyst.* **12**, 12009 (2011).
8. D. McKenzie, *J. Petrol.* **25**, 713–765 (1984).
9. R. Katz, *J. Petrol.* **49**, 2099 (2008).
10. R. Katz, *Geochem. Geophys. Geosyst.* **10**, Q0AC07 (2010).
11. R. Katz, S. Weatherley, *Earth Planet. Sci. Lett.* **335–336**, 226–237 (2012).
12. A. Stracke, B. Bourdon, D. McKenzie, *Earth Planet. Sci. Lett.* **244**, 97–112 (2006).
13. Materials and methods are available as supplementary materials on Science Online.
14. M. Siddall, B. Hönisch, C. Waelbroeck, P. Huybers, *Quat. Sci. Rev.* **29**, 170–181 (2010).
15. I. Hewitt, *Earth Planet. Sci. Lett.* **300**, 264–274 (2010).
16. J. D. Hays, J. Imbrie, N. J. Shackleton, *Science* **194**, 1121–1132 (1976).
17. C. DeMets, R. G. Gordon, D. F. Argus, *Geophys. J. Int.* **181**, 1–80 (2010).
18. D. Percival, A. Walden, *Spectral Analysis for Physical Applications: Multitaper and Conventional Univariate Techniques* (Cambridge Univ. Press, Cambridge, UK, 1993).
19. P. Huybers, C. Wunsch, *Paleoceanography* **19**, PA1028 (2004).
20. W. R. Buck, L. L. Lavier, A. N. Poliakov, *Nature* **434**, 719–723 (2005).

## ACKNOWLEDGMENTS

The research leading to these results has received funding from the European Research Council (ERC) under the European Union's

Seventh Framework Programme (FP7/2007–2013)/ERC grant agreement 279925 and from the U.S. National Science Foundation under grant 1338832. It is a part of project PPI3040 and PEI4050 funded by the Korea Polar Research Institute. J.W.C. thanks J. Mitrovica, and R.F.K. thanks the Leverhulme Trust for additional support. Numerical models were run at Oxford's Advanced Research Computing facility. Bathymetry data are included in the supplementary materials.

## SUPPLEMENTARY MATERIALS

www.sciencemag.org/content/347/6227/1237/suppl/DC1

Figs. S1 to S3

Table S1

References (21–29)

Data Files KRL and KR2

22 September 2014; accepted 28 January 2015

10.1126/science.1261508

## EPIDEMIOLOGY

# Reduced vaccination and the risk of measles and other childhood infections post-Ebola

Saki Takahashi,<sup>1</sup> C. Jessica E. Metcalf,<sup>1,2</sup> Matthew J. Ferrari,<sup>3</sup> William J. Moss,<sup>4</sup> Shaun A. Truelove,<sup>4</sup> Andrew J. Tatem,<sup>5,6,7</sup> Bryan T. Grenfell,<sup>1,6</sup> Justin Lessler<sup>4\*</sup>

The Ebola epidemic in West Africa has caused substantial morbidity and mortality. The outbreak has also disrupted health care services, including childhood vaccinations, creating a second public health crisis. We project that after 6 to 18 months of disruptions, a large connected cluster of children unvaccinated for measles will accumulate across Guinea, Liberia, and Sierra Leone. This pool of susceptibility increases the expected size of a regional measles outbreak from 127,000 to 227,000 cases after 18 months, resulting in 2000 to 16,000 additional deaths (comparable to the numbers of Ebola deaths reported thus far). There is a clear path to avoiding outbreaks of childhood vaccine-preventable diseases once the threat of Ebola begins to recede: an aggressive regional vaccination campaign aimed at age groups left unprotected because of health care disruptions.

The current Ebola crisis in West Africa is one of the worst public health disasters in recent memory, having caused more than 21,000 cases and 8400 deaths as of January 2015 and raising the specter of a broader international crisis (1). However, there are signs of hope. Evidence shows that the number of cases is declining in Liberia (2), and sustained transmission has been confined to Guinea, Liberia, and Sierra Leone, despite several transnational introductions including recent transmission in Mali. Stopping Ebola would be a triumph for the global health community and the public health agencies of the affected countries. But even after the last Ebola case recovers, the disruptions of

local health systems caused by the outbreak could lead to a second infectious disease crisis that could kill as many as, if not more than, the original outbreak.

Through the combination of the World Health Organization (WHO) Expanded Programme on Immunization (EPI) and periodic supplemental immunization campaigns, annual childhood deaths from vaccine-preventable diseases have dropped from an estimated 900,000 in 2000 to 400,000 in 2010 (3). Measles is emblematic of this success; globally, estimated annual measles mortality has decreased from 499,000 to 102,000 since 2000 (4, 5). The Ebola-affected countries have been an important part of this achievement: The three countries reported nearly 93,685 cases of measles in the decade between 1994 and 2003 (despite Sierra Leone not reporting in 4 years), and only 6937 between 2004 and 2013 (in both periods it is likely that only a fraction of measles cases were reported to the WHO) (6). Despite this success, measles susceptibility has been growing in all three countries in recent years, and each had planned a measles vaccination campaign prior to the Ebola outbreak.

Measles epidemics often follow humanitarian crises. Measles is one of the most transmissible infections, and immunization rates tend to be lower than for other EPI vaccines, in part because of the older age at which measles vaccine must be administered [9 months, versus 6 weeks or younger for the first dose of other vaccines (7)]. For this reason, explosive measles outbreaks are often an early result of health system failure. Outbreaks have followed disruptions due to war [e.g., the current conflict in Syria (8)], natural disasters [e.g., the eruptions of Mt. Pinatubo in 1991 (9)], and political crises [e.g., Haiti in the early 1990s (10)]. The effects are most acute when measles epidemics are associated with famine or long-term national instability: A survey of 595 households displaced as a result of the Ethiopian famine in 2000 found measles to be a contributing cause in 35 of 159 deaths (11), and after years of instability in the Democratic Republic of Congo, the country experienced a measles outbreak of 294,455 cases and 5045 deaths between 2010 and 2013 (12).

To understand how Ebola-related health care disruptions are increasing the risk from measles, we estimated the spatial distribution of unvaccinated children and the measles susceptibility profile for each country before and after these disruptions. Geolocated cross-sectional data from Demographic and Health Surveys (DHS) in Guinea, Liberia, Sierra Leone, and surrounding countries were used to estimate vaccine coverage in each 5 km × 5 km grid cell by means of a hierarchical Bayesian model and spatial smoothing techniques. These rates were applied to spatially explicit data on population and birth cohort size to map the number of children between 9 months and 5 years of age who were unvaccinated against measles before Ebola-related health care disruptions (Fig. 1A) (13, 14). Forward projections of the number of unvaccinated children after 6, 12, and 18 months were generated by reducing the rate of routine vaccination by 75% for the specified duration (reductions of 25, 50, and 100% were also considered as a sensitivity analysis). Full population susceptibility on a national level at baseline and after 18 months of disruptions were then estimated by combining these estimates with the results of models that estimate the immune profile in each age cohort on the basis of their

<sup>1</sup>Department of Ecology and Evolutionary Biology, Princeton University, Princeton, NJ 08544, USA. <sup>2</sup>Woodrow Wilson School, Princeton University, Princeton, NJ 08544, USA.

<sup>3</sup>Centre for Infectious Disease Dynamics, Pennsylvania State University, State College, PA 16801, USA. <sup>4</sup>Department of Epidemiology, Johns Hopkins Bloomberg School of Public Health, Baltimore, MD 21205, USA. <sup>5</sup>Department of Geography and Environment, University of Southampton, Southampton SO17 1BJ, UK. <sup>6</sup>Fogarty International Center, National Institutes of Health, Bethesda, MD 20892, USA.

<sup>7</sup>Flowminder Foundation, 17177 Stockholm, Sweden.

\*Corresponding author. E-mail: justin@jhu.edu